Check for updates

ADVANCING EARTH AND SPACE SCIENCES

JGR Atmospheres

RESEARCH ARTICLE

10.1029/2023JD039062

Subdaily Extreme Precipitation and Its Linkage to Global Warming Over the Tibetan Plateau

Mengnan Ma[1,2], Jianping Tang[1,2], Tinghai Ou[3], and Deliang Chen[3]

[1]Key Laboratory of Mesoscale Severe Weather/Ministry of Education, Nanjing University, Nanjing, China, [2]School of Atmospheric Sciences, Nanjing University, Nanjing, China, [3]Department of Earth Sciences, Regional Climate Group, University of Gothenburg, Gothenburg, Sweden

Key Points:

- The simulated hourly precipitation over the Tibetan Plateau (TP) is characterized by heterogeneity and spatially disparate changes
- Less frequent, shorter duration, and more intense precipitation over the southeastern and the southern border of the TP are projected
- The distributions of the intensity-related indices exhibit a dependency on elevation

Supporting Information:

Supporting Information may be found in the online version of this article.

Correspondence to:

J. Tang,
jptang@nju.edu.edu

Citation:

Ma, M., Tang, J., Ou, T., & Chen, D. (2023). Subdaily extreme precipitation and its linkage to global warming over the Tibetan Plateau. *Journal of Geophysical Research: Atmospheres*, *128*, e2023JD039062. https://doi.org/10.1029/2023JD039062

Received 13 APR 2023
Accepted 28 AUG 2023

© 2023. American Geophysical Union. All Rights Reserved.

Abstract The spatiotemporal characteristics of subdaily extreme precipitation over the Tibetan Plateau (TP) have undergone significant changes due to global warming. In this study, we employed the high-resolution Weather Research and Forecasting regional climate model to conduct a series of historical and projection simulations under representative concentration pathways (RCPs), especially RCP4.5 and RCP8.5. The aim was to investigate the past and future climatologies and spatiotemporal evolution of subdaily precipitation extremes using newly proposed subdaily extreme precipitation indices (EPIs). The results show that projected changes in precipitation amount, particularly during wet hours, exhibit spatial disparities. Notably, there are significant decreases along the southern border of the TP and over the western TP, while obvious increases are observed over the inner TP. The southeastern TP, western TP, and southern border of the TP are expected to experience less frequent, shorter duration, and more intense precipitation on an hourly basis. The TP, as a whole, has demonstrated significantly increasing trends in moderate-to-heavy precipitation frequencies, along with consistent decreasing trends in precipitation events with short, medium, and long durations. Furthermore, it is predicted that the relationship between extreme precipitation and temperature will deviate from the Clausius-Clapeyron (C-C) relationship toward the double C-C relationship in the far-future under RCP8.5, particularly over the southeastern TP. Additionally, there are robust correlations between the intensity-related EPIs and elevation. This indicates that, at the local scale, the complex topography of the region may play a crucial role in shaping the nonuniform distribution of precipitation extremes by modulating associated upward motion.

Plain Language Summary The Tibetan Plateau (TP) has experienced substantial warming during the past decades, at a rate twice that of the global average due to its unique location and elevated terrain. Warming has significantly changed the amount, intensity, frequency, and extremes of precipitation over the TP. The changes in precipitation would influence the stability of the local ecoenvironment and the development of agriculture and industry directly. Previous studies have shown the big picture of daily precipitation extremes in the future, but the characteristics of precipitation extremes at hourly timescale are unclear. This study simulates the changes in subdaily precipitation extremes in the historical (1980–2005) and future (2006–2099) periods under different climate scenarios (RCP4.5 and RCP8.5). Our results show that the spatiotemporal changes and variability over the western TP, the southern border of TP and the southeastern TP are more dramatic than that over the central TP. The southeastern TP shows higher sensitivity and vulnerability to subdaily precipitation extremes and may experience less frequent precipitation lasting for a shorter duration, but with stronger intensity at hourly timescale. The results of this study can guide adaptive measures and be helpful for long-term water resource management over the TP.

1. Introduction

According to the Intergovernmental Panel on Climate Change (IPCC) Sixth Assessment Report (AR6), the global surface temperature from 2011 to 2020 was 1.09°C higher than that from 1850 to 1900 (IPCC, 2022). The Tibetan Plateau (TP), known as the Third Pole (Qiu, 2008; Yao et al., 2012), has experienced accelerated warming since the second half of the twentieth century (Kuang & Jiao, 2016), which was earlier (Kang et al., 2010; Liu & Chen, 2000) and faster than that over the Northern Hemisphere (Yao et al., 2019; Zhou & Zhang, 2021). This significant warming has profoundly changed the amount, intensity, frequency, type, and extremes of precipitation (Cao & Pan, 2014). In recent decades, precipitation changes over the TP have exhibited large regional discrepancies and temporal variability (Cuo et al., 2013; Gao et al., 2014, 2015; You et al., 2012), with the in situ observed

10.1029/2023JD039062

annual precipitation increasing in most areas of the TP and decreasing in the eastern and southeastern parts during the period 1979–2011 (Gao et al., 2015; Kuang & Jiao, 2016).

Increasing hydrological extremes (Ding et al., 2021; Yang et al., 2014; You et al., 2008) and the increasing trend of the contribution of extreme rainfall to the total precipitation (Ge et al., 2017) have been reported over the TP. Consequent floods, droughts, and snowstorms caused by increasing extreme precipitation events have had an adverse effect on ecosystems, agriculture, infrastructure, and socioeconomic development (He et al., 2021; Ward et al., 2020). Therefore, the occurrences of extreme precipitation events and their trends have become the focus of most climate change studies (Xiong et al., 2019; Yang et al., 2012).

Daily precipitation extremes do appear to be increasing in magnitude and frequency at the global and continental scales (Asadieh & Krakauer, 2015; Donat et al., 2016). In particular, subdaily precipitation extremes are more sensitive to warming than daily precipitation extremes (Ali & Mishra, 2018; Barbero et al., 2018; Chinita et al., 2021) and more accurately reflect the intermittency of the precipitation (Trenberth et al., 2017). This seems to be a property of convective precipitation and may be attributed to the release of latent heat within convective storms invigorating vertical motion, which is thought to generate greater increases in hourly rainfall intensities (Lenderink et al., 2017).

Although the characteristics of and changes in the subdaily precipitation extremes in many parts of the world, such as Europe (Chan et al., 2014; Lavin-Gullon et al., 2021; Pichelli et al., 2021), North America (Barbero et al., 2017), and parts of China (Xiao et al., 2016), have been well established, it is still unclear how subdaily precipitation extremes are shaped and have evolved over the TP. Li and Yu (2014) analyzed the frequency-intensity distribution of the hourly precipitation based on rain gauge data and found that the frequency of light rain was higher and that the number of intense rainfall events was smaller at stations with high altitudes and complex orography compared to those on the plains of eastern China. Furthermore, through analysis of hourly rain gauge records, Li (2018) found that extreme precipitation events tended to start in the late afternoon and terminated in the morning, and the precipitation over the southeastern TP was characterized by a large amount, high frequency, and strong intensity. Although the projection of the daily mean and extreme precipitation over the TP has been extensively studied under the background of significant warming, the problem of projecting the changes in the subdaily precipitation and its extremes is still open for discussion.

Theoretically, water vapor increases tend to be governed by the Clausius-Clapeyron (C-C) relationship to temperature, but extreme precipitation changes are more complex due to dynamical feedbacks (Neelin et al., 2022). This relationship indicates that the water-holding capacity of the air will increase by approximately 7% per degree of warming (Park & Min, 2017; Trenberth, 2011). However, the scaling rates of extreme precipitation and temperature are strongly dependent on the region (Prein et al., 2017; Wasko & Sharma, 2017), temperature (Utsumi et al., 2011), and moisture availability (Chan et al., 2016). The super-C-C scaling has been interpreted in connection with convective precipitation (Lenderink et al., 2017), which is highly relevant to midlatitude regions in the warm season when convective precipitation represents an important proportion of the total amount (e.g., over the TP). It has also been discovered that the relationship between temperature and extreme precipitation may change with the precipitation duration (hourly, daily, and multiday) (Shaw et al., 2011; Yong et al., 2021). However, evaluating the effects of warming on subdaily precipitation extremes in regions with complex orography based on the surface station network is particularly challenging due to limitations such as data inhomogeneity, missing data, and various biases associated with the measurement processes (Guerreiro et al., 2018).

As stated in the IPCC AR6, high-resolution climate models are needed to increase confidence in climate projections (IPCC, 2021). However, reliable simulation of precipitation extremes and their attribution to warming at the regional scale remain challenging. In general, a higher model resolution is an important step toward further including more small-scale processes (Ma et al., 2021, 2023a; Zhou et al., 2022). For dynamic reasons, many properties of the severe storms responsible for extreme precipitation cannot be resolved at coarse grid spacings, regardless of how good the subgrid-scale physical parameterizations are (Wehner et al., 2021). In addition, inferring the hourly precipitation amounts from observational data sets (e.g., remote sensing and gauge network) is difficult because satellite estimates may be strongly affected by clouds and surface properties, and in situ observations may be insufficient in terms of the demand for temporal and spatial resolution. However, data merging exploiting the complementary strengths of gauge, satellite, and reanalysis-based precipitation estimates are very promising (Barbero et al., 2019).

In this study, we focus on the aforementioned questions in order to present a comprehensive understanding of the projected subdaily extreme precipitation over the TP. The goals of this study were (a) to identify the spatiotemporal

21698996, 2023, 18, Downloaded from https://agupubs.onlinelibrary.wiley.com/doi/10.1029/2023JD039062 by Goteborgs, Wiley Online Library on [12/09/2023]. See the Terms and Conditions (https://onlinelibrary.wiley.com/terms-and-conditions) on Wiley Online Library for rules of use; OA articles are governed by the applicable Creative Commons License

Journal of Geophysical Research: Atmospheres
10.1029/2023JD039062

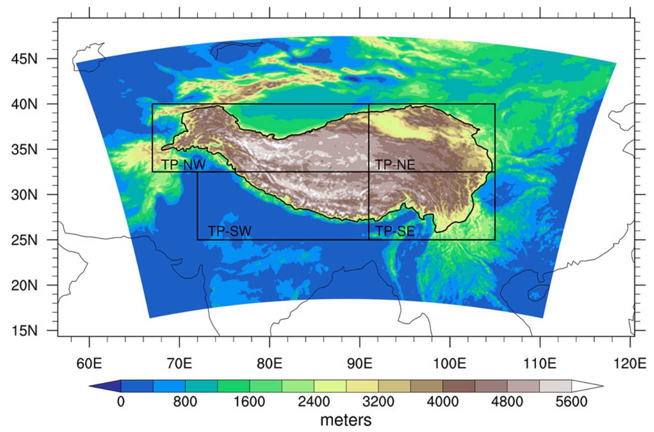

Figure 1. The simulation domain of the WRF (shading). The subregions are framed by black rectangles, and the name of the region is noted in the bottom-left corner of each rectangle.

changes in the subdaily precipitation extremes in the near-future (2020–2039), mid-future (2040–2059), and far-future (2080–2099) over the TP; and (b) to investigate its thermodynamic response to warming and deviation from the C-C rate due to dynamic factors.

The remainder of this article is organized as follows. Section 2 describes the model and experimental design, data, and methodology. Section 3 presents the main results concerning the projected changes in subdaily precipitation extremes. The thermodynamic and dynamic aspects are discussed in Section 4. Section 5 summarizes the conclusions obtained in this study.

2. Data and Methods

2.1. Model Setup and Experimental Design

The WRF with Advanced Research (ARW) dynamic core version 4.1.1 (Skamarock et al., 2019), configured with 361 × 531 grid points in the north-south and east-west directions, using a 9 km horizontal grid spacing to encompass the entire TP and part of its surrounding areas (Figure 1), is used. There are 40 hybrid-sigma levels with an upper boundary of 50 hPa. The parameterization schemes employed are the Thompson microphysics scheme (Thompson et al., 2008), the Yonsei University (YSU) planetary boundary layer (PBL) parameterization (Hong et al., 2006), the rapid radiative transfer model for general circulation model (RRTMG) shortwave and longwave radiation schemes (Iacono et al., 2008), and the Unified Noah Land Surface Model (Mukul Tewari et al., 2004). No cumulus parameterizations are used.

The global climate model (GCM) forcing data used in this paper originates from the CESM (Hurrell et al., 2013) provided by the National Center for Atmospheric Research (NCAR). The bias-corrected CESM outputs following the mean-bias-correction method (Bruyère et al., 2014) are generated for dynamic downscaling of the WRF simulation. The bias-correction method corrects the mean state while retaining the synoptic-scale and climate-scale variability simulated by the CESM, which have been proven to be critical for regional climate modeling over the TP (Zhu et al., 2019). Additionally, spectral nudging is applied to the wind field above the planetary boundary level, with the nudging wavenumber of four in both directions and nudging coefficient of 3×10^{-4} that corresponds to the time scale about 1 hr.

A set of dynamically downscaled WRF simulations is conducted from 1979 to 2100 continuously and is forced by the 6-hr bias-corrected CESM output fields. The first year is treated as the spin-up that is broadly defined as an adjustment process as the model approaches its equilibrium with minimal artificial drift in the model state or prognostic variables (Cosgrove et al., 2003), without which the uncertainties can propagate from the beginning of the modeling chain to the final simulations, and the results can be misleading (Yang et al., 1995); thus, the spin-up time is excluded from analysis. Several periods are chosen to represent the historical (1980–2005), near-future (2020–2039), mid-future (2040–2059), and far-future (2080–2099) climate. For the future (2006–2100) projections, RCP4.5 and RCP8.5 are chosen to examine the influence of a middle and high emission scenario on high-impact weather events. The historical WRF simulation (1980–2005) was previously evaluated (Ma et al., 2023c), showing good agreement between mean and extreme temperature and precipitation simulations and observations.

2.2. Hourly Extreme Precipitation Indices

Subdaily extreme precipitation indices (EPIs) (Alexander et al., 2019) produced by the Intelligent Use of Climate Models for Adaptation to Non-Stationary Hydrological Extremes (INTENSE) project (Blenkinsop et al., 2018) are used to quantify the nature of the rainfall extremes. The indices are grouped into three classes, mainly based on the aspects they can measure and their computational algorithms, enabling a thorough examination of subdaily precipitation extremes in terms of frequency, intensity and duration. The classification generally follows that in Li et al. (2022), and details of the selected indices are presented in Table 1. It should be noted that a wet spell is allowed to span multiple days. In this paper, all of the time series of EPIs are computed and examined for an entire year.

In addition, the precipitation events are classified according to their duration with measurable hourly precipitation of ≥0.1 mm/hr following the methods of Li (2018) and Yu et al. (2007). The duration of a precipitation event is the number of hours from the beginning to the end of the event. Each precipitation event can contain a maximum of one

21698996, 2023, 18, Downloaded from https://agupubs.onlinelibrary.wiley.com/doi/10.1029/2023JD039062 by Goteborgs, Wiley Online Library on [12/09/2023]. See the Terms and Conditions (https://onlinelibrary.wiley.com/terms-and-conditions) on Wiley Online Library for rules of use; OA articles are governed by the applicable Creative Commons License

21698996, 2023, 18, Downloaded from https://agupubs.onlinelibrary.wiley.com/doi/10.1029/2023JD039062 by Goteborgs, Wiley Online Library on [12/09/2023]. See the Terms and Conditions (https://onlinelibrary.wiley.com/terms-and-conditions) on Wiley Online Library for rules of use; OA articles are governed by the applicable Creative Commons License

Table 1
Hourly Extreme Precipitation Indices Selected in This Study

Type of index	Index	Description	Definition	Units
Intensity-related indices	Rx1hr	Maximum 1 hr precipitation	Maximum 1 hr precipitation	mm
	Rx3hr	Maximum 3 hr precipitation	Maximum 3 hr precipitation	mm
	Rx6hr	Maximum 6 hr precipitation	Maximum 6 hr precipitation	mm
Frequency-related indices	R1hr5mm	Number of moderate-to-heavy precipitation hours	Number of hours with hourly precipitation of ≥5 mm	hrs
Duration-related indices	MxLWS	Maximum consecutive wet hours	Maximum number of consecutive wet hours	hrs
	MeLWS	Average consecutive wet hours	Average number of consecutive wet hours	hrs
General indices	RTot	Total wet-hour precipitation	Total precipitation during wet hours	mm
	NWH	Wet-hour frequency	Number of wet hours	hrs
	SPII1hr	Hourly precipitation intensity	Ratio of the total wet-hour precipitation to the number of wet hours	mm/hr

Note. A wet hour is defined as an hour with a precipitation rate of ≥0.1 mm.

1-hr gap (i.e., when the hourly precipitation is less than 0.1 mm). Precipitation events that last for 1–3 hr, 4–6 hr, and longer than 6 hr are classified as short-duration, medium-duration, and long-duration events, respectively.

2.3. Statistical Method

The nonparametric Mann-Kendall (MK) test (Kendall, 1948; Mann, 1945) is applied to the long-term time series to detect statistical significance of the trend. The MK test has been widely used in analyzing the significance of EPIs' trends (Bhatti et al., 2020; Tramblay et al., 2013). In this paper, the trend is considered to be statistically significant if it reaches either the 0.01 or 0.05 significance level. The magnitude of the trend in a given time series is determined using Sen's nonparametric estimator method (Sen, 1968).

The scaling of the extreme precipitation with temperature is expressed by the relationship between the 99th percentile of the daily maximum hourly precipitation (P99_dmax) and the daily average temperature following the method of Knist et al. (2020). First, at each grid point, the daily maximum hourly precipitation over the investigated period is attributed to the daily mean temperature over the same period sorted into 1°C bins, with 80 bins selected to cover a wide range of temperature values. Then, for each temperature bin, only if there are more than 100 samples, are they counted, and the 99th percentile of the precipitation values (P99_dmax) is calculated. The P99_dmax values are then averaged over the grid points in the particular analysis region. Thus, the extreme precipitation-temperature (EP-T) relationship curves can be obtained. Furthermore, to ensure a more representative EP-T scaling, the end-tail of the curves with lower temperature bins are discarded due to a smaller number of grid points available for averaging in those specific subregions, accounting for less than 20% of the total grid points. Specifically, only when 50% of the grid points have statistical P99_dmax values are the EP-T scaling curves calculated at a specific temperature bin.

Composite analysis, recognized as an effective technique for identifying the conditions observed during specific climate states and providing valuable information about the physical mechanisms involved (Boschat et al., 2016), is applied. Here, we first identify the precipitation events at each time interval. Further, the diagnostic w component of wind on mass points is extracted at 500 and 300 hPa to construct the composite vertical velocity field corresponding to the identified subdaily precipitation events occurring in the same period.

3. Results

3.1. Changes in EPI Distributions

3.1.1. General Indices

Figure 2 depicts the spatial distributions of RTot, NWH, and SPII1hr from the historical period and their projected changes in the far-future, as well as the differences between RCP4.5 and RCP8.5. These indices measure the total precipitation, precipitation frequency, and average precipitation intensity of the hourly precipitation processes, providing an overall view of the hourly precipitation characteristics.

10.1029/2023JD039062

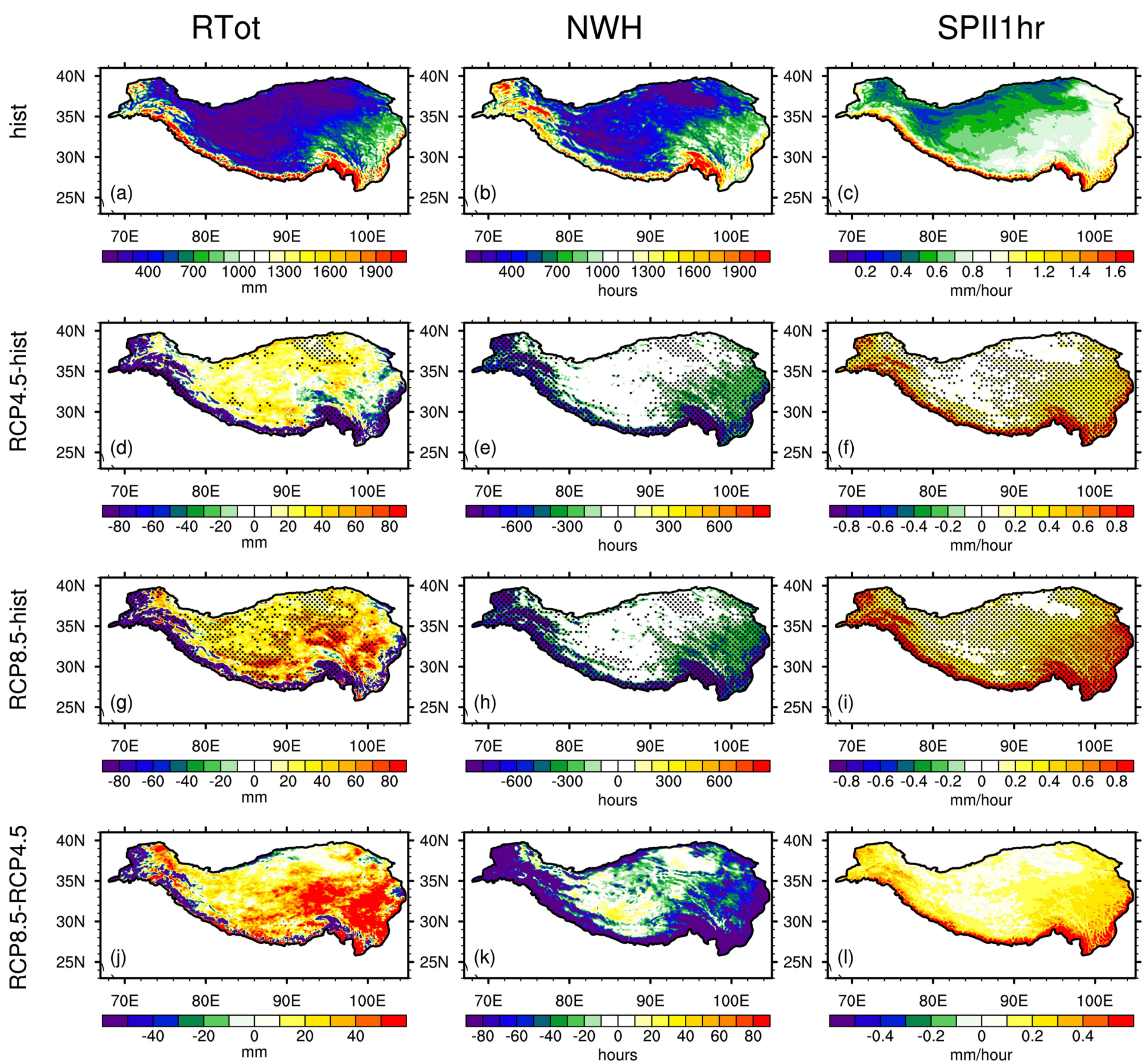

Figure 2. Spatial distribution of 26 years mean (1980–2005) RTot, NWH, and SPII1hr from the historical run (first row); projected changes in the RTot, NWH, and SPII1hr in the far-future under RCP4.5/RCP8.5 (second/third row); and differences between RCP4.5 and RCP8.5 (fourth row). The projected changes passing the significance test at the 99% confidence level are dotted.

Since the projected changes in the near- and mid-future are not as significant as those in the far-future, and the general spatial features are similar to those in the far-future, they are not highlighted here. The climatology of RTot, NWH, and SPII1hr from the historical run decreases from southeast to northwest over the inner TP, while the southeastern TP and the southern border of the TP are faced with the most total precipitation during the wet hours, the most wet hours, and the most intense hourly precipitation.

In the far-future, the RTot will increase by approximately 20–40 mm over the majority of the central and northwestern TP, while it will decrease by more than 80 mm over the southern border of the TP (Figures 2d and 2g). Over the southeastern TP, the projected changes in RTot under RCP4.5 and RCP8.5 differ, with dominant decrease under RCP4.5 but increase under RCP8.5. In contrast to RTot, which will exhibit nonuniform spatial changes and a divergent projection over specific areas under two RCP scenarios, coherent decrease of NWH and increase of SPII1hr are projected under both RCP scenarios, with the most obvious changes occurring over the southeastern

21698996, 2023, 18, Downloaded from https://agupubs.onlinelibrary.wiley.com/doi/10.1029/2023JD039062 by Goteborgs, Wiley Online Library on [12/09/2023]. See the Terms and Conditions (https://onlinelibrary.wiley.com/terms-and-conditions) on Wiley Online Library for rules of use; OA articles are governed by the applicable Creative Commons License

21698996, 2023, 18, Downloaded from https://agupubs.onlinelibrary.wiley.com/doi/10.1029/2023JD039062 by Goteborgs, Wiley Online Library on [12/09/2023]. See the Terms and Conditions (https://onlinelibrary.wiley.com/terms-and-conditions) on Wiley Online Library for rules of use; OA articles are governed by the applicable Creative Commons License

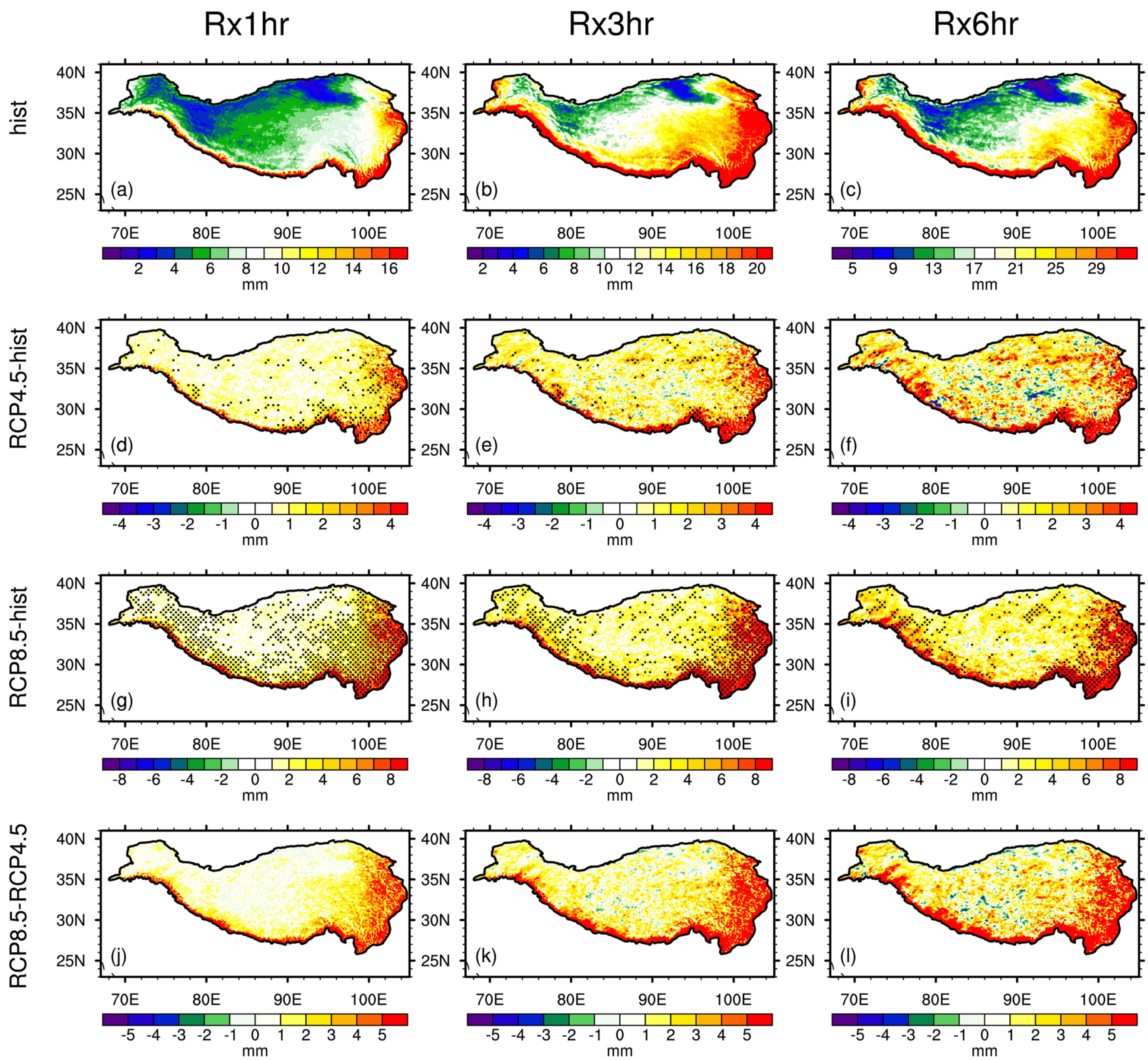

Figure 3. Spatial distribution of 26 years mean (1980–2005) Rx1hr, Rx3hr, and Rx6hr from the historical run (first row); projected changes in Rx1hr, Rx3hr, and Rx6hr in the far-future under RCP4.5/RCP8.5 (second/third row); and differences between RCP4.5 and RCP8.5 (fourth row). The projected changes that pass the significance test at the 99% confidence level are dotted.

TP and the southern border of the TP. Thus, the significant decrease in RTot over the southern border of the TP is attributed to the stronger decrease in NWH. However, over the southeastern TP, the predominant increase in RTot under RCP8.5 may be influenced more by the significant increase in SPII1hr, while the decrease under RCP4.5 may be related more closely to the decrease in NWH.

3.1.2. Frequency-Related and Intensity-Related Indices

Figure 3 shows the spatial distributions of Rx1hr, Rx3hr, and Rx6hr from the historical run and their projected changes in the far-future, as well as the differences between RCP4.5 and RCP8.5. Temporally, the precipitation peak always occurs at approximately 16:00–17:00 Local Standard Time (LST) according to the diurnal cycle of the precipitation (figure not shown) in both the historical period and future projection. Rx1hr, Rx3hr, and Rx6hr exhibit similar spatial patterns decreasing from southeast to northwest, with the maxima occurring over the eastern TP and along the southern border of the TP (Figures 3a–3c). The northwestern TP and the Qaidam Basin

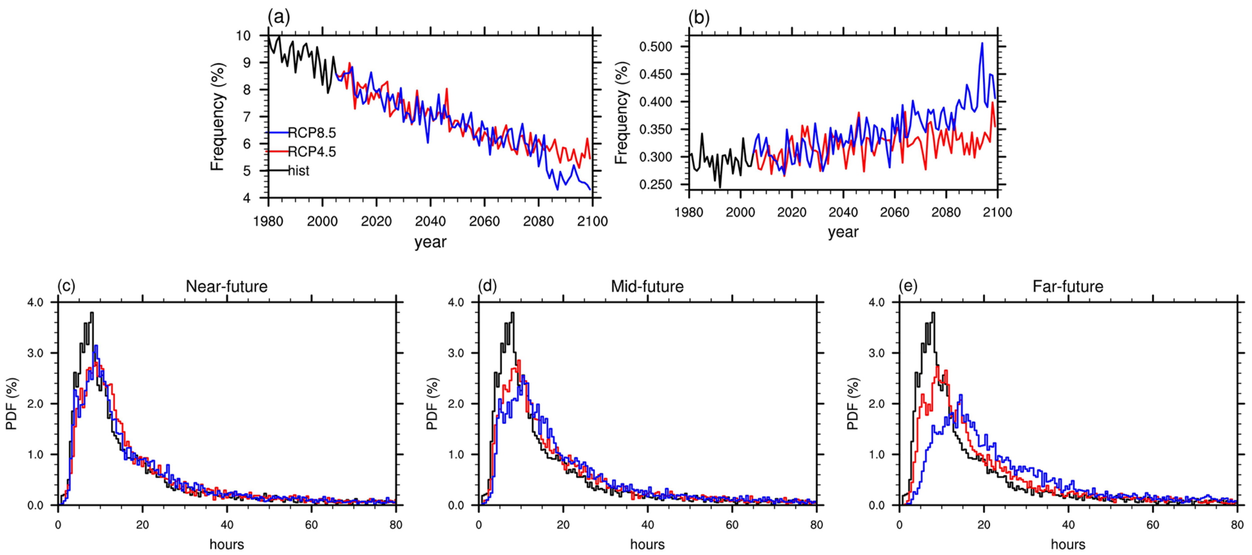

Figure 4. Time evolution of regional mean precipitation frequency over the Tibetan Plateau (TP) for precipitation amounts of <5 mm (a) and ≥5 mm (b) in the historical period and the future under RCP4.5/RCP8.5. Probability distribution functions (PDFs) of R1hr5mm over the southeastern TP in the (c) near-future, (d) mid-future, and (e) far-future under RCP4.5/RCP8.5 compared with that in the historical period.

are characterized by weaker hourly precipitation intensity. In the far-future, under RCP4.5, Rx1hr is projected to nonuniformly increase by more than 2.0 mm over the eastern TP, and the increase in the amplitude will be approximately twice as large under RCP8.5. For Rx3hr and Rx6hr, majority parts of the TP will be faced with intensified precipitation, while some parts of the central TP will experience decreases under RCP4.5 (Figures 3e and 3f). Inhomogenous increase in the precipitation intensity is also projected under RCP8.5 (Figures 3g–3i).

The regional mean precipitation frequency over the TP for light precipitation (less than 5 mm/hr) is projected to decrease significantly until the end of the 21st century, while the frequency of moderate-to-heavy precipitation (≥5 mm/hr) is projected to increase significantly (both at the 99% confidence level) during the same period (Figure 4). Therefore, the projected changes in the distribution of R1hr5mm, representing the number of hours with hourly precipitation ≥5 mm, are investigated. Spatially, the projected changes in R1hr5mm are similar to those of the intensity-related indices, with the eastern and southern TP experiencing more frequent moderate-to-heavy precipitation. The projected changes in the probability distribution function (PDF) of R1hr5mm over the southeastern TP in the future under the RCP scenarios are shown in Figure 4. Quantitatively, the annual total hours with precipitation of ≥5 mm is within 50 for most grid points (Figures 4c–4e), which mostly occurs in summer. A rightward shift in the PDF occurs under both RCP scenarios and is more evident in the far-future.

Generally, the more humid areas in climate, such as the eastern TP, southern TP, and the southern border of the TP, will experience dramatic increases in the extreme precipitation frequency and stronger intensity at the hourly scale. This also agrees well with the big picture, that is, increases in the frequency and intensity of the daily precipitation extremes over the TP, predicted in previous studies (Gao et al., 2018; Hui et al., 2022; Yang et al., 2012).

3.1.3. Duration-Related Indices

First, the characteristics of precipitation events with different durations at the hourly scale are depicted in Figure 5. The precipitation over the southeastern TP is mainly characterized by short-duration (Figure 5a), while that along the southern border of the TP and over the western TP is characterized by long-duration (Figure 5c). Under the background of warming, the short-duration, medium-duration, and long-duration precipitation events, as well as the mean duration of each precipitation event, are projected to gradually and coherently decrease. For the short-duration and medium-duration precipitation events, the most dramatic decreases will occur over the southeastern TP and some parts of the southern border of the TP, with more than 50 annually (Figures 5d, 5e, 5g, and 5h). In contrast, the southwestern TP and Qaidam Basin are projected to experience slight increases in short-duration events (Figures 5d and 5g). For the long-duration events, the western TP will be more severely challenged, with a decrease of more than 10 events annually (Figures 5f and 5i). Most short-duration precipitation events end in the afternoon (in local time), while medium-duration and long-duration precipitation events ends

21698996, 2023, 18, Downloaded from https://agupubs.onlinelibrary.wiley.com/doi/10.1029/2023JD039062 by Goteborgs, Wiley Online Library on [12/09/2023]. See the Terms and Conditions (https://onlinelibrary.wiley.com/terms-and-conditions) on Wiley Online Library for rules of use; OA articles are governed by the applicable Creative Commons License

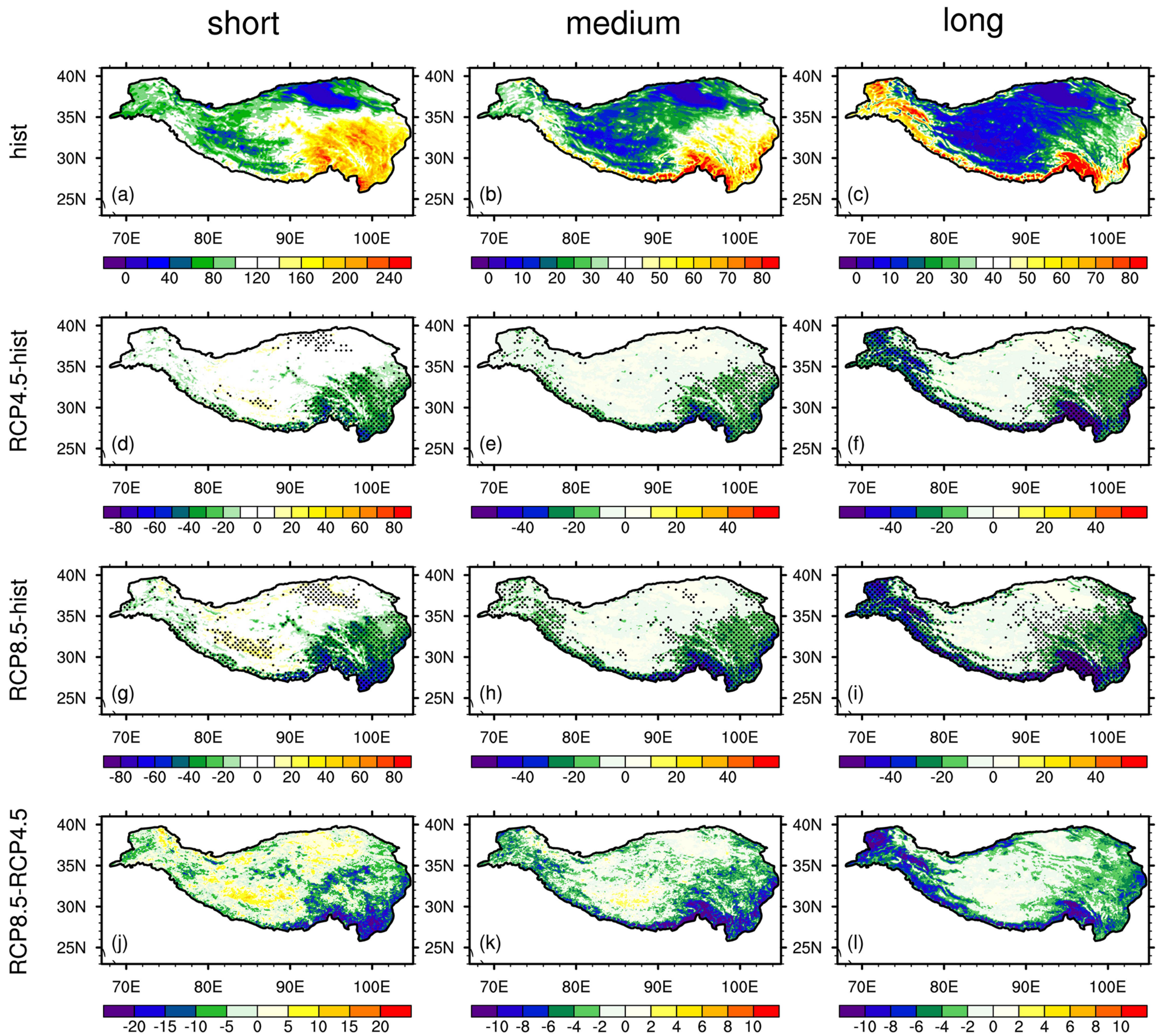

Figure 5. Spatial distribution of 26 years mean (1980–2005) short-duration, medium-duration, and long-duration precipitation events from the historical run (first row); projected changes in the short-duration, medium-duration, and long-duration precipitation events in the far-future under RCP4.5/RCP8.5 (second/third row); and differences between RCP4.5 and RCP8.5 (fourth row). The projected changes that pass the significance test at the 99% confidence level are dotted.

in the early morning based on the historical simulation (figure not shown), which will remain almost unchanged in the future. This indicates that the response of the hourly precipitation to warming is probably reflected by the increase in the intensity of each precipitation event and the decrease in the frequency of events.

The spatial distributions of MeLWS and MxLWS in the historical period and under the two RCP scenarios are illustrated in Figure 6. According to the historical simulation, the maximum MeLWS above 6 hrs, and the maximum MxLWS above 50 hrs occur over the western TP and along the southern border of the TP, while the minimum MeLWS below 2.5 hrs, and the minimum MxLWS below 15 hrs occur over the central TP and Qaidam Basin (Figures 6a and 6e). Under the background of warming, general decreases in MeLWS and MxLWS are projected, especially over the eastern TP and along the southern border of the TP (Figures 6b, 6c, 6f, and 6g).

Based on the analysis above, the precipitation over the southeastern TP and along the southern border of the TP will tend to occur less frequently, continue for a shorter duration, and have a larger intensity. Furthermore, the moderate-to-heavy precipitation frequency will increase, increasing the risk of floods and droughts.

21698996, 2023, 18, Downloaded from https://agupubs.onlinelibrary.wiley.com/doi/10.1029/2023JD039062 by Goteborgs, Wiley Online Library on [12/09/2023]. See the Terms and Conditions (https://onlinelibrary.wiley.com/terms-and-conditions) on Wiley Online Library for rules of use; OA articles are governed by the applicable Creative Commons License

10.1029/2023JD039062

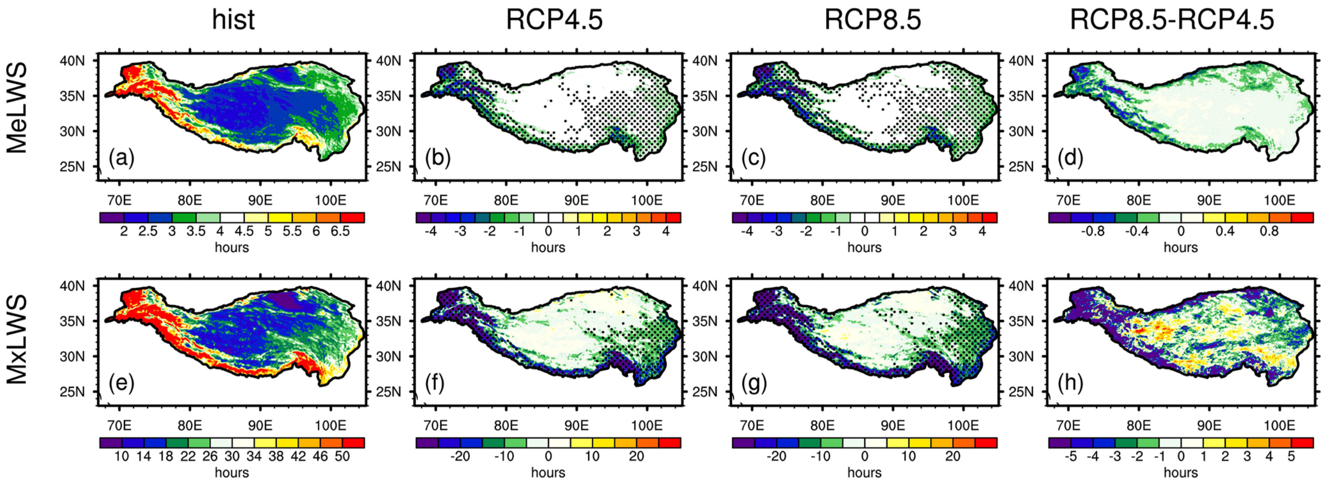

Figure 6. Spatial distribution of 26 years mean (1980–2005) MeLWS and MxLWS from the historical run (first row); projected changes in MeLWS and MxLWS in the far-future under RCP4.5/RCP8.5 (second/third row); and differences between RCP4.5 and RCP8.5 (fourth row). The projected changes that pass the significance test at the 99% confidence level are dotted.

3.2. Trends and Interannual Variability of EPIs

3.2.1. General Indices

The RTot trend is spatially disparate, with the increasing trend greater over the inner TP under RCP8.5 (Figure S1 in Supporting Information S1). Along the southern border of the TP, the decreasing trends are greater than 10 mm/decade (Figures S1a and S1b in Supporting Information S1). The NWH is projected to significantly decrease at a rate of more than 60 hr/decade over the western TP and along the southern border of the TP under RCP4.5 where the decreasing trend under RCP8.5 is approximately 20 hr/decade faster (Figures S1d–S1f in Supporting Information S1). SPII1hr is projected to increase at the fastest rate of more than 0.1 mm/hr/decade in these regions (Figures S1g–S1i in Supporting Information S1). Therefore, the southeastern TP and the southern border of the TP will undergo the most dramatic changes in NWH and SPII1hr, with significantly faster rates and stronger interannual variabilities that are characterized by larger standard deviation values (Figure S2 in Supporting Information S1). Temporally, the regional mean NWH is projected to decrease at a rate of approximately 24.4 hr/decade under RCP4.5 and 31.9 hr/decade under RCP8.5, and the regional mean SPII1hr is projected to increase at a rate of approximately 0.05 mm/hr/decade under RCP4.5 and 0.07 mm/hr/decade under RCP8.5 (Figure S3 in Supporting Information S1 and Table 2). Since the RTot trend exhibits a large spatial inhomogeneity, the temporal characteristics of the regional mean RTot are not shown in Table 2 and are not discussed here.

Table 2
Trends of Hourly Extreme Precipitation Indices and Precipitation Events With Different Duration During 2006–2099

	RCP4.5	RCP8.5
NWH	−24.41 hr/decade*	−31.91 hr/decade**
SPII1hr	0.046 mm/hr/decade**	0.069 mm/hr/decade**
Rx1hr	0.14 mm/decade**	0.45 mm/decade**
Rx3hr	0.25 mm/decade**	0.74 mm/decade**
Rx6hr	0.33 mm/decade**	0.93 mm/decade**
R1hr5mm	0.15 hr/decade**	0.50 hr/decade**
MeLWS	−0.061 hr/decade**	−0.085 hr/decade**
MxLWS	−0.96 hr/decade**	−1.28 hr/decade**
Short-duration	−1.46 events/decade**	−1.58 events/decade**
Medium-duration	−1.57 events/decade*	−1.36 events/decade*
Long-duration	−1.38 events/decade**	−1.74 events/decade**

Note. The statistics in the second/third column represents the trend under RCP4.5/RCP8.5. */** denotes that the trend is significant at the 95%/99% confidence level.

3.2.2. Frequency-Related and Intensity-Related Indices

The spatial distributions of the intensity-related indices' trends under RCP4.5 and RCP8.5 are characterized by faster increasing trends over the eastern TP (Figure S4 in Supporting Information S1). The increasing trends are within 0.5 mm/decade under RCP4.5, while they are approximately 1.0 mm/decade faster under RCP8.5. According to the time series of intensity-related indices (Figure S3 in Supporting Information S1), the increasing trends remain almost the same under RCP4.5 and RCP8.5 in the beginning. However, they start to diverge in 2040, and then, the difference between them further widens in 2060, which is earlier than the timing for the general indices. The eastern TP is projected to experience strong interannual variability (above 10.0 mm) (Figure S5 in Supporting Information S1).

21698996, 2023, 18, Downloaded from https://agupubs.onlinelibrary.wiley.com/doi/10.1029/2023JD039062 by Goteborgs, Wiley Online Library on [12/09/2023]. See the Terms and Conditions (https://onlinelibrary.wiley.com/terms-and-conditions) on Wiley Online Library for rules of use; OA articles are governed by the applicable Creative Commons License

21698996, 2023, 18, Downloaded from https://agupubs.onlinelibrary.wiley.com/doi/10.1029/2023JD039062 by Goteborgs, Wiley Online Library on [12/09/2023]. See the Terms and Conditions (https://onlinelibrary.wiley.com/terms-and-conditions) on Wiley Online Library for rules of use; OA articles are governed by the applicable Creative Commons License

Table 3
The Correlation Coefficients Between Intensity-Related Indices and Precipitation Events With Different Duration, as Well as That Between Intensity-Related Indices and Mean Duration of Each Precipitation Event During 2006–2099

	Rx1hr (mm)	Rx3hr (mm)	Rx6hr (mm)
Short-duration	−0.57**/−0.84**	−0.29**/−0.57**	−0.26*/−0.54**
Medium-duration	−0.60**/−0.86**	−0.55**/−0.84**	−0.48**/−0.80**
Long-duration	−0.73**/−0.91**	−0.66**/−0.89**	−0.57**/−0.84**
Mean duration (hour)	−0.74**/−0.90**	−0.66**/−0.87**	−0.56**/−0.82**

Note. The former/latter statistics in each cell of the second, third, and fourth column represents the correlation coefficients under RCP4.5/RCP8.5. */** denotes that the trend is significant at the 95%/99% confidence level.

For R1hr5mm, the faster increasing trends (>2 hr/decade) and stronger interannual variability (>10 hr) coexist over the southeastern TP and along the southern border of the TP under RCP8.5 (figure not shown). Since trends at most grid points do not pass the significance test at the 99% confidence level, they are thought to change as not significantly as intensity-related indices.

3.2.3. Duration-Related Indices

Consistent decreasing trends of short-duration, medium-duration, and long-duration precipitation events are projected over the southeastern TP and along the southern border of the TP (Figure S6 in Supporting Information S1). The western TP will experience a significant decrease in the number of long-duration precipitation events, with a rate of greater than 3 events/decade. The decreasing trends of short-duration, medium-duration, and long-duration precipitation events under RCP4.5 and RCP8.5 start to diverge greatly after the 2080s (Figure S3 in Supporting Information S1). The southeastern TP exhibit strong interannual variability, exceeding 20 for short-duration precipitation and 10 for medium-duration and long-duration precipitation events (Figure S7 in Supporting Information S1). The short-duration precipitation events over the central-eastern TP and the long-duration precipitation events over the western TP also exhibit strong interannual variability.

For the duration-related EPIs, the faster decreasing trends and stronger interannual variability are distributed over the western TP and along the southern border of the TP, especially for MxLWS (Figure S8 in Supporting Information S1). More dramatic decreases are projected to occur after the 2080s under RCP8.5 (Figure S3 in Supporting Information S1).

3.3. Possible Relationship Between EPIs and Elevation Dependency

Furthermore, it was found that the intensity-related indices have a notable dependency on elevation (Figure S9 in Supporting Information S1). There are robust negative correlations between them that are significant at the 99% confidence level based on the two-sided t test. The correlation coefficients (r) between the intensity-related indices and elevation range from −0.50 to −0.40 for Rx1hr, −0.48 to −0.35 for Rx3hr, and −0.45 to −0.34 for Rx6hr. The correlations tend to become higher in the future, especially under RCP8.5. The interannual variability of these indices is also closely related to elevation, reaching approximately −0.54 in the historical run, −0.56/−0.56 in the near-future, −0.56/−0.56 in the mid-future, and −0.56/−0.57 in the far-future under RCP4.5/RCP8.5 (significant at the 99% confidence level). These reveal that elevation is also an important factor affecting the variability of precipitation extremes over the TP.

Investigation into the intensity-related indices and precipitation events with different durations revealed that there is a robust negative correlation between them (Table 3). Rx1hr is highly correlated with the numbers of short-duration, medium-duration, and long-duration precipitation events, as well as the mean duration of precipitation events. The higher Rx1hr is, the shorter the mean duration of precipitation events is. Rx3hr and Rx6hr are closely correlated with the numbers of medium- and long-duration precipitation events and mean duration of precipitation events, but the correlations are not as high as those with Rx1hr. Although the occurrence of precipitation events with different durations and their mean duration is correlated with the intensity-related indices, they are not highly correlated with the topographic heightlike intensity-related indices do, with the absolute value of the correlation coefficients below 0.3.

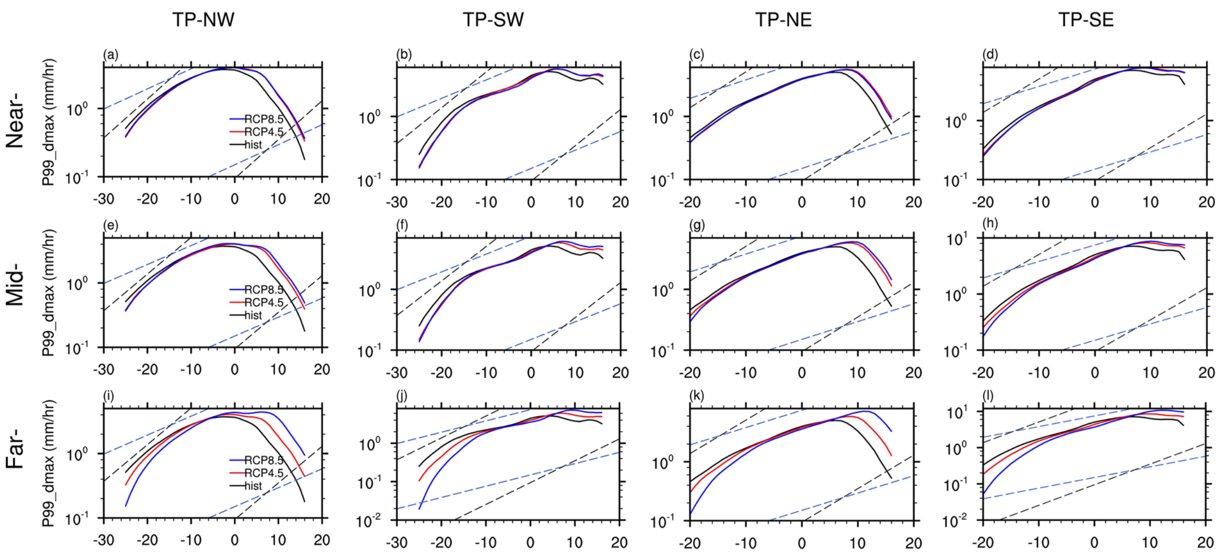

Figure 7. Hourly precipitation extremes (99th percentile) versus daily averaged future temperature over different subregions of TP, as is denoted at the top of each column. Light blue and gray dashed lines indicate 1 and 2 times of the C-C scaling, respectively. The unit of temperature: °C.

4. Discussion

The amount of precipitable water over the TP is much lower than that in the surrounding areas due to its elevated land surface. Thus, the precipitation is largely controlled by the availability of water vapor, which is closely related to warming. Another important factor modulating the subdaily precipitation characteristics is the complex local topography, which exerts an important influence on terrain-induced local circulations. Therefore, the thermodynamic and dynamic changes over the TP under the background of warming are discussed in this section.

4.1. EP-T Scaling

Figure 7 shows the historical and future EP-T scaling in the four subregions of the TP. In the historical simulation, the EP-T curves exhibit a hook-like structure in all subregions. Over the northwestern TP (TP-NW), the EP-T relationship in the historical simulation exceeds the C-C scaling by approximately 1%/K at temperatures ranging from approximately −26°C to the turning point that corresponds to the maximum P99_dmax value. Over the southwestern TP (TP-SW), the EP-T relationship generally follows the C-C scaling, which is approximately 6.2%/K, at temperatures ranging from approximately −19°C to the turning point. Over the northeastern TP (TP-NE) and southeastern TP (TP-SE), the turning point of the temperature for extreme precipitation is higher than that over the western TP, which can reach approximately 8°C. The EP-T scaling is also larger than that over the western TP, exceeding the C-C scaling by approximately 2%/K from −20°C to the turning point over the TP-NE and from −16°C to the turning point over the TP-SE, respectively. In all subregions, a negative EP-T scaling was detected when the temperature was above the turning point, and an increase in temperature does not necessarily favor extreme precipitation because of moisture limitations (Jones & Randall, 2011; Neelin et al., 2009).

The shapes of the EP-T curves under RCP4.5 and RCP8.5 in the future are similar to that from the historical simulation, except for a shift toward higher temperature and higher extreme precipitation peaks, especially under RCP8.5. Over the TP-NW and TP-NE, the EP-T scaling is around 10%/K under both RCP scenarios. Over the TP-SW, the EP-T scaling will slightly exceed the C-C scaling by 1~2%/K. The TP-SE has the largest EP-T scaling (~10%/K) after the near-future, and it tends to develop toward the double C-C scaling in the far-future under RCP8.5 (~12%/K). This reveals that the southeastern TP will be more sensitive to warming in the far-future, which may partially explain the predominant increase in RTot in this area.

4.2. Large-Scale Vertical Velocity

In addition to the increasing atmospheric moisture content under a warming climate (Allen & Ingram, 2002; Trenberth, 1999), extreme precipitation is also influenced by other thermodynamic and dynamic properties such

21698996, 2023, 18, Downloaded from https://agupubs.onlinelibrary.wiley.com/doi/10.1029/2023JD039062 by Goteborgs, Wiley Online Library on [12/09/2023]. See the Terms and Conditions (https://onlinelibrary.wiley.com/terms-and-conditions) on Wiley Online Library for rules of use; OA articles are governed by the applicable Creative Commons License

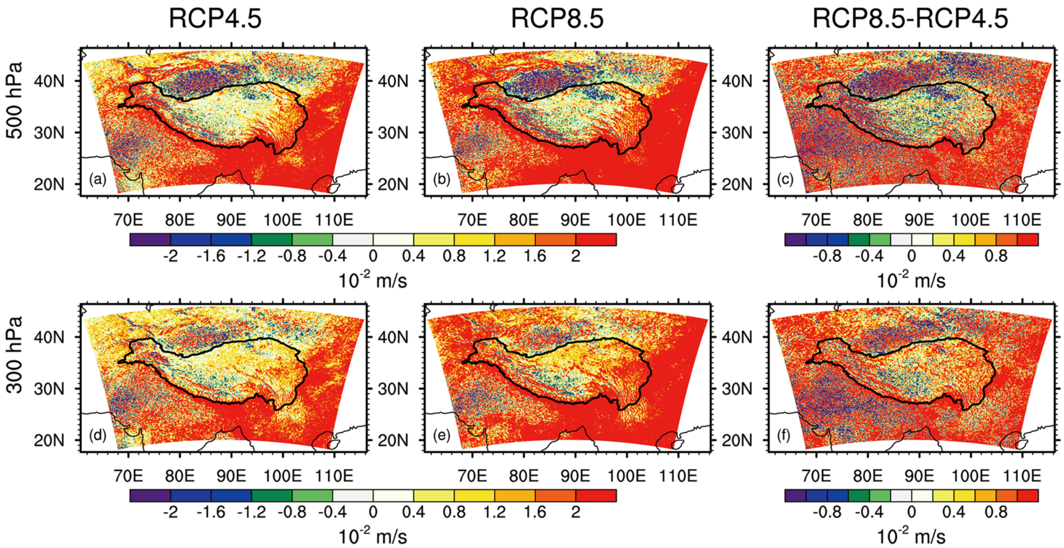

Figure 8. Projected changes in composite vertical velocity in the far-future at 500 and 300 hPa under RCP4.5 (the first row), RCP8.5 (the second row) and differences between RCP4.5 and RCP8.5 (the third row).

as intensified water recycling (Nie & Sun, 2022; Zhang et al., 2023), changes in the temperature lapse rate and vertical wind velocities (Pfahl et al., 2017; Sugiyama et al., 2010; O'Gorman & Schneider, 2009). On regional scales, dynamic factors and local factors such as topography can make the response of precipitation extremes more complex, especially when convection is important (O'Gorman, 2015).

There is a link between large-scale vertical velocities, which are associated with large-scale atmospheric conditions, and subdaily extreme precipitation intensities (Lenderink et al., 2017). Figure 8 shows the projected changes in the composite vertical velocity at 500 hPa and 300 hPa in the far-future under RCP4.5 and RCP8.5. The spatial pattern of the projected changes in the composite vertical velocity at low-levels and mid-levels is similar to that of Rx1hr (Figure 3). The increase in the upward motion is mainly projected in the areas where Rx1hr, Rx3hr, and Rx6hr are also projected to intensify. This indicates that hourly precipitation extremes are on average accompanied by substantial large-scale upward motions. Correlation analysis was conducted to obtain a comprehensive understanding of the robustness of relevance between the composite vertical velocity and intensity-related indices (Table S1 in Supporting Information S1). The projected changes in the composite vertical velocity at both low-levels and mid-levels are related to the changes in the intensity-related indices, but the composite vertical velocity at the low-level exhibits a higher correlation with the intensified hourly precipitation than that at the mid-level. The correlation coefficients between changes in composite vertical velocity in the low-level and changes in the intensity-related indices are greater than 0.50 (all significant at the 99% confidence level), with values above 0.60 under RCP8.5.

It is found that the increased latent heating, especially over the southeastern TP (figure not shown), which is triggered to counterbalance the global warming-driven increases in surface and troposphere temperatures, may be the cause of intensified upward motions (Trenberth, 2011). The stronger upward motion induces condensation and precipitation formation which in turn release latent heat, hence establishing the positive feedback between the upward motion and precipitation/diabatic heating, which is also theoretically established and observationally recorded in previous studies (Nie et al., 2018; Tandon et al., 2018). Though a brief mechanistic interpretation of the feedbacks between the thermodynamic and dynamic factors to intensified precipitation is provided here, it is certainly not all of the story, with the roles of other processes (e.g., changes in cloud entrainment and cloud-aerosol interactions) not well understood at current stage (Fowler et al., 2021). More in-depth studies are required to gain additional insight into these processes that are responsible for the modulation of subdaily precipitation extremes.

Investigation in this section provides more evidence for the hypothesis that at the local scale, the topography may play an important role in making the response of precipitation extremes more complicated through its modulation of the terrain-induced circulation and the associated upward motion. Stronger upward motion over the

21698996, 2023, 18, Downloaded from https://agupubs.onlinelibrary.wiley.com/doi/10.1029/2023JD039062 by Goteborgs, Wiley Online Library on [12/09/2023]. See the Terms and Conditions (https://onlinelibrary.wiley.com/terms-and-conditions) on Wiley Online Library for rules of use; OA articles are governed by the applicable Creative Commons License

21698996, 2023, 18, Downloaded from https://agupubs.onlinelibrary.wiley.com/doi/10.1029/2023JD039062 by Goteborgs, Wiley Online Library on [12/09/2023]. See the Terms and Conditions (https://onlinelibrary.wiley.com/terms-and-conditions) on Wiley Online Library for rules of use; OA articles are governed by the applicable Creative Commons License

eastern TP and along the southern border of the TP has been shown to have a robust correlation with intensified hourly precipitation. The intensified hourly precipitation there will further lead to a reduction in the numbers of short-duration, medium-duration, and long-duration precipitation events.

5. Conclusions and Discussions

In this study, using the high-resolution WRF model, a series of historical simulation and projections under RCP4.5 and RCP8.5 were conducted. The projected changes in the spatial pattern, trend and variability of the subdaily extreme precipitation as well as the thermodynamic and dynamic conditions were investigated.

Regarding the general indices, it is projected that RTot will undergo heterogeneous changes. Increases in RTot are expected over the majority of the central and northwestern TP, while decreases are projected along the southern border of the TP. Consistent decrease in NWH and increase in SPII1hr are observed under both RCP scenarios. Moreover, these changes exhibit a faster trend and stronger interannual variability over the southeastern TP and along the southern border of the TP.

In terms of the frequency-related and intensity-related indices, the most intense precipitation is projected to occur over the eastern TP and along the southern border of the TP. The frequency of the moderate-to-heavy precipitation is expected to increase significantly, indicating that more grid points over the eastern TP will face an elevated risk of heavy rain.

Regarding the duration-related indices, coherent decreases are projected for precipitation events with short, medium, and long durations. The southeastern TP is expected to face dramatic decreases in short-duration and medium-duration precipitation events, while the western TP will see a reduction in long-duration precipitation events. Consequently, general decreases in MeLWS and MxLWS are projected, particularly over the eastern TP and along the southern border of the TP.

Under the context of global warming, the EP-T curves are expected to shift toward a higher temperature and higher peaks of extreme precipitation. This shift indicates that the EP-T scaling will further deviate from the C-C scaling, particularly over the southeastern TP under RCP8.5, potentially following a double C-C scaling in the far-future. The higher sensitivity of the southeastern TP to warming may partially explain the more pronounced changes in subdaily precipitation in this area.

Additionally, the close relationship between increased upward vertical velocities and intensified subdaily precipitation highlights the significance of topography in shaping the spatial pattern of the intensified subdaily precipitation.

Furthermore, it is important to note that downscaled regional climate projections are subject to various sources of uncertainty. One of the uncertainties is related to gray-zone modeling. Nonhydrostatic dynamics cannot be accurately represented with horizontal resolutions larger than 4 km, beyond which convective mass flux may be overestimated, leading to the production of "grid-scale storms" (Weisman et al., 1997). This can result in overestimated precipitation due to convective instability forced onto an unrealistically coarser scale (Prein et al., 2015). Other poorly understood feedbacks at the gray-zone scale, such as cloud-radiative feedbacks and cloud-aerosol interactions that depend on accurate representations of clouds, may also introduce uncertainties.

Another source of uncertainty is associated with the regional climate model (RCM) and downscaling process itself. Different RCMs driven by the same GCM can produce considerably different climate change signals (Giorgi, 2019). Thus, accounting for uncertainties in the RCM itself, as well as those transferred from the GCM, is essential. Several studies focusing on the climate projections over the TP have employed multi-RCM ensemble downscaled by various GCMs to address these uncertainties (e.g., Fu et al., 2021; Niu et al., 2021). However, generating climate projections based on ensembles at a convection-permitting scale remains challenging due to computational limitations, although it is expected to help further reduce uncertainties. Additionally, uncertainties can arise from factors such as emission scenarios, land use change, internal climate variability, and other sources.

Data Availability Statement

The bias-corrected CESM outputs (Hurrell et al., 2013) are available via https://rda.ucar.edu/datasets/ds316.1/. The WRF model (Skamarock et al., 2019), used to generate the historical simulation and future projections in this study, is available from https://www.mmm.ucar.edu/weather-research-and-forecasting-model. The data generated and used in this study can be accessed with the identifier DOI: https://doi.org/10.5281/zenodo.7812878 (Ma et al., 2023b).

Acknowledgments
The research is supported by the Second Tibetan Plateau Scientific Expedition and Research Program (STEP, Grant 2019QZKK0206), the National Key Research and Development Program of China (2018YFA0606003), the National Natural Science Foundation of China (41875124), the Swedish Foundation for International Cooperation in Research and Higher Education (CH2020-8767), and Swedish Research Council (VR-2019-03954).

References

Alexander, L. V., Fowler, H. J., Bador, M., Behrangi, A., Donat, M. G., Dunn, R., et al. (2019). On the use of indices to study extreme precipitation on sub-daily and daily timescales. *Environmental Research Letters*, *14*(12), 125008. https://doi.org/10.1088/1748-9326/ab51b6

Ali, H., & Mishra, V. (2018). Increase in subdaily precipitation extremes in India under 1.5 and 2.0°C warming worlds. *Geophysical Research Letters*, *45*, 6972–6982. https://doi.org/10.1029/2018GL078689

Allen, M. R., & Ingram, W. J. (2002). Constraints on future changes in climate and the hydrologic cycle. *Nature*, *419*(6903), 224–232. https://doi.org/10.1038/nature01092

Asadieh, B., & Krakauer, N. Y. (2015). Global trends in extreme precipitation: Climate models versus observations. *Hydrology and Earth System Sciences*, *19*(2), 877–891. https://doi.org/10.5194/hess-19-877-2015

Barbero, R., Fowler, H. J., Blenkinsop, S., Westra, S., Moron, V., Lewis, E., et al. (2019). A synthesis of hourly and daily precipitation extremes in different climatic regions. *Weather and Climate Extremes*, *26*, 100219. https://doi.org/10.1016/j.wace.2019.100219

Barbero, R., Fowler, H. J., Lenderink, G., & Blenkinsop, S. (2017). Is the intensification of precipitation extremes with global warming better detected at hourly than daily resolutions? *Geophysical Research Letters*, *44*, 974–983. https://doi.org/10.1002/2016GL071917

Barbero, R., Westra, S., Lenderink, G., & Fowler, H. (2018). Temperature-extreme precipitation scaling: A two-way causality? *International Journal of Climatology*, *38*(S1), e1274–e1279. https://doi.org/10.1002/joc.5370

Bhatti, A. S., Wang, G., Ullah, W., Ullah, S., Fiifi Tawia Hagan, D., Kwesi Nooni, I., et al. (2020). Trend in extreme precipitation indices based on long term in situ precipitation records over Pakistan. *Water*, *12*(3), 797. https://doi.org/10.3390/w12030797

Blenkinsop, S., Fowler, H. J., Barbero, R., Chan, S. C., Guerreiro, S. B., Kendon, E., et al. (2018). The INTENSE project: Using observations and models to understand the past, present and future of sub-daily rainfall extremes. *Advances in Science and Research*, *15*, 117–126. https://doi.org/10.5194/asr-15-117-2018

Boschat, G., Simmonds, I., Purich, A., Cowan, T., & Pezza, A. B. (2016). On the use of composite analyses to form physical hypotheses: An example from heat wave – SST associations. *Scientific Reports*, *6*(1), 29599. https://doi.org/10.1038/srep29599

Bruyère, C. L., Done, J. M., Holland, G. J., & Fredrick, S. (2014). Bias corrections of global models for regional climate simulations of high-impact weather. *Climate Dynamics*, *43*(7–8), 1847–1856. https://doi.org/10.1007/s00382-013-2011-6

Cao, L., & Pan, S. (2014). Changes in precipitation extremes over the "Three-River Headwaters" region, hinterland of the Tibetan Plateau, during 1960–2012. *Quaternary International*, *321*, 105–115. https://doi.org/10.1016/j.quaint.2013.12.041

Chan, S. C., Kendon, E. J., Fowler, H. J., Blenkinsop, S., & Roberts, N. M. (2014). Projected increases in summer and winter UK sub-daily precipitation extremes from high-resolution regional climate models. *Environmental Research Letters*, *9*(8), 084019. https://doi.org/10.1088/1748-9326/9/8/084019

Chan, S. C., Kendon, E. J., Roberts, N. M., Fowler, H. J., & Blenkinsop, S. (2016). Downturn in scaling of UK extreme rainfall with temperature for future hottest days. *Nature Geoscience*, *9*(1), 24–28. https://doi.org/10.1038/ngeo2596

Chinita, M. J., Richardson, M., Teixeira, J., & Miranda, P. M. A. (2021). Global mean frequency increases of daily and sub-daily heavy precipitation in ERA5. *Environmental Research Letters*, *16*(7), 074035. https://doi.org/10.1088/1748-9326/ac0caa

Cosgrove, B. A., Lohmann, D., Mitchell, K. E., Houser, P. R., Wood, E. F., Schaake, J. C., et al. (2003). Land surface model spin-up behavior in the north American land data Assimilation System (NLDAS). *Journal of Geophysical Research*, *108*(D22), 8845. https://doi.org/10.1029/2002JD003316

Cuo, L., Zhang, Y., Wang, Q., Zhang, L., Zhou, B., Hao, Z., & Su, F. (2013). Climate change on the northern Tibetan plateau during 1957–2009: Spatial patterns and possible mechanisms. *Journal of Climate*, *26*(1), 85–109. https://doi.org/10.1175/JCLI-D-11-00738.1

Ding, J., Cuo, L., Zhang, Y., Zhang, C., Liang, L., & Liu, Z. (2021). Annual and seasonal precipitation and their extremes over the Tibetan plateau and its surroundings in 1963–2015. *Atmosphere*, *12*(5), 620. https://doi.org/10.3390/atmos12050620

Donat, M. G., Lowry, A. L., Alexander, L. V., O'Gorman, P. A., & Maher, N. (2016). More extreme precipitation in the world's dry and wet regions. *Nature Climate Change*, *6*(5), 508–513. https://doi.org/10.1038/nclimate2941

Fowler, H. J., Lenderink, G., Prein, A. F., Westra, S., Allan, R. P., Ban, N., et al. (2021). Anthropogenic intensification of short-duration rainfall extremes. *Nature Reviews Earth & Environment*, *2*(2), 107–122. https://doi.org/10.1038/s43017-020-00128-6

Fu, Y.-H., Gao, X.-J., Zhu, Y.-M., & Guo, D. (2021). Climate change projection over the Tibetan Plateau based on a set of RCM simulations. *Advances in Climate Change Research*, *12*(3), 313–321. https://doi.org/10.1016/j.accre.2021.01.004

Gao, Y., Cuo, L., & Zhang, Y. (2014). Changes in moisture flux over the Tibetan plateau during 1979–2011 and possible mechanisms. *Journal of Climate*, *27*(5), 1876–1893. https://doi.org/10.1175/JCLI-D-13-00321.1

Gao, Y., Li, X., Ruby Leung, L., Chen, D., & Xu, J. (2015). Aridity changes in the Tibetan Plateau in a warming climate. *Environmental Research Letters*, *10*(3), 034013. https://doi.org/10.1088/1748-9326/10/3/034013

Gao, Y., Xiao, L., Chen, D., Xu, J., & Zhang, H. (2018). Comparison between past and future extreme precipitations simulated by global and regional climate models over the Tibetan Plateau. *International Journal of Climatology*, *38*(3), 1285–1297. https://doi.org/10.1002/joc.5243

Ge, G., Shi, Z., Yang, X., Hao, Y., Guo, H., Kossi, F., et al. (2017). Analysis of precipitation extremes in the Qinghai-Tibetan plateau, China: Spatio-temporal characteristics and topography effects. *Atmosphere*, *8*(12), 127. https://doi.org/10.3390/atmos8070127

Giorgi, F. (2019). Thirty years of regional climate modeling: Where are we and where are we going next? *Journal of Geophysical Research: Atmospheres*, *124*, 5696–5723. https://doi.org/10.1029/2018JD030094

Guerreiro, S. B., Fowler, H. J., Barbero, R., Westra, S., Lenderink, G., Blenkinsop, S., et al. (2018). Detection of continental-scale intensification of hourly rainfall extremes. *Nature Climate Change*, *8*(9), 803–807. https://doi.org/10.1038/s41558-018-0245-3

He, Q., Yang, J., Chen, H., Liu, J., Ji, Q., Wang, Y., & Tang, F. (2021). Evaluation of extreme precipitation based on three long-term gridded products over the Qinghai-Tibet plateau. *Remote Sensing*, *13*(15), 3010. https://doi.org/10.3390/rs13153010

Hong, S.-Y., Noh, Y., & Dudhia, J. (2006). A new vertical diffusion package with an explicit treatment of entrainment processes. *Monthly Weather Review*, *134*(9), 2318–2341. https://doi.org/10.1175/mwr3199.1

Hui, P., Wei, F., Xiao, Y., Yang, J., Xu, J., & Tang, J. (2022). Future projection of extreme precipitation within CORDEX east Asia phase II: Multi-model ensemble. *Theoretical and Applied Climatology*, *150*(3–4), 1271–1293. https://doi.org/10.1007/s00704-022-04223-0

Hurrell, J. W., Holland, M. M., Gent, P. R., Ghan, S., Kay, J. E., Kushner, P. J., et al. (2013). The Community Earth System model: A framework for Collaborative research[Dataset]. Bulletin of the American Meteorological Society, *94*(9), 1339–1360. https://doi.org/10.1175/bams-d-12-00121.1

21698996, 2023, 18, Downloaded from https://agupubs.onlinelibrary.wiley.com/doi/10.1029/2023JD039062 by Goteborgs, Wiley Online Library on [12/09/2023]. See the Terms and Conditions (https://onlinelibrary.wiley.com/terms-and-conditions) on Wiley Online Library for rules of use; OA articles are governed by the applicable Creative Commons License

Iacono, M. J., Delamere, J. S., Mlawer, E. J., Shephard, M. W., Clough, S. A., & Collins, W. D. (2008). Radiative forcing by long-lived greenhouse gases: Calculations with the AER radiative transfer models. *Journal of Geophysical Research*, *113*, D13103. https://doi.org/10.1029/2008JD009944

IPCC. (2021). Summary for policymakers. In V.Masson-Delmotte, P.Zhai, A.Pirani, C. Connors, S. Péan, N. Berger, et al. (Eds.), *Climate change 2021: The physical science basis. Contribution of working group I to the sixth assessment report of the intergovernmental panel on climate change* (pp. 1–41). Cambridge University Press.

IPCC, (2022). Climate change 2022: Impacts, adaptation, and vulnerability. In H.-O. Pörtner, D. C. Roberts, M. Tignor, E. S. Poloczanska, K. Mintenbeck, A. Alegría, et al. (Eds.), *Contribution of working group II to the Sixth assessment report of the intergovernmental panel on climate change* (pp. 3056). Cambridge University Press. https://doi.org/10.1017/9781009325844

Jones, T. R., & Randall, D. A. (2011). Quantifying the limits of convective parameterizations. *Journal of Geophysical Research*, *116*, D08210. https://doi.org/10.1029/2010jd014913

Kang, S., Xu, Y., You, Q., Flügel, W.-A., Pepin, N., & Yao, T. (2010). Review of climate and cryospheric change in the Tibetan Plateau. *Environmental Research Letters*, *5*(1), 015101. https://doi.org/10.1088/1748-9326/5/1/015101

Kendall, M. G. (1948). *Rank correlation methods*. Griffin.

Knist, S., Goergen, K., & Simmer, C. (2020). Evaluation and projected changes of precipitation statistics in convection-permitting WRF climate simulations over Central Europe. *Climate Dynamics*, *55*(1), 325–341. https://doi.org/10.1007/s00382-018-4147-x

Kuang, X., & Jiao, J. J. (2016). Review on climate change on the Tibetan Plateau during the last half century. *Journal of Geophysical Research: Atmospheres*, *121*, 3979–4007. https://doi.org/10.1002/2015JD024728

Lavin-Gullon, A., Feijoo, M., Solman, S., Fernandez, J., Da Rocha, R. P., & Bettolli, M. L. (2021). Synoptic forcing associated with extreme precipitation events over Southeastern South America as depicted by a CORDEX FPS set of convection-permitting RCMs. *Climate Dynamics*, *56*(9–10), 3187–3203. https://doi.org/10.1007/s00382-021-05637-8

Lenderink, G., Barbero, R., Loriaux, J. M., & Fowler, H. J. (2017). Super-Clausius-Clapeyron scaling of extreme hourly convective precipitation and its relation to large-scale atmospheric conditions. *Journal of Climate*, *30*(15), 6037–6052. https://doi.org/10.1175/JCLI-D-16-0808.1

Li, J. (2018). Hourly station-based precipitation characteristics over the Tibetan Plateau. *International Journal of Climatology*, *38*(3), 1560–1570. https://doi.org/10.1002/joc.5281

Li, J., & Yu, R. (2014). A method to linearly evaluate rainfall frequency–intensity distribution. *Journal of Applied Meteorology and Climatology*, *53*(4), 928–934. https://doi.org/10.1175/jamc-d-13-0272.1

Li, X., Zhang, K., Bao, H., & Zhang, H. (2022). Climatology and changes in hourly precipitation extremes over China during 1970-2018. *Science of the Total Environment*, *839*, 156297. https://doi.org/10.1016/j.scitotenv.2022.156297

Liu, X., & Chen, B. (2000). Climatic warming in the Tibetan Plateau during recent decades. *International Journal of Climatology: A Journal of the Royal Meteorological Society*, *20*(14), 1729–1742. https://doi.org/10.1002/1097-0088(20001130)20:14<1729::AID-JOC556>3.0.CO;2-Y

Ma, M., Hui, P., Liu, D., Zhou, P., & Tang, J. (2021). Convection-permitting regional climate simulations over Tibetan plateau: Re-initialization versus spectral nudging. *Climate Dynamics*, *58*(5–6), 1719–1735. https://doi.org/10.1007/s00382-021-05988-2

Ma, M., Ou, T., Liu, D., Wang, S., Fang, J., & Tang, J. (2023a). Summer regional climate simulations over Tibetan plateau: From gray zone to convection permitting scale. *Climate Dynamics*, *60*(1–2), 301–322. https://doi.org/10.1007/s00382-022-06314-0

Ma, M., Tang, J., Ou, T., & Chen, D. (2023b). Sub-daily extreme precipitation and its linkage to global warming over the Tibetan plateau [Dataset]. Zenodo. https://doi.org/10.5281/zenodo.7812878

Ma, M., Tang, J., Ou, T., & Zhou, P. (2023c). High-resolution climate projection over the Tibetan Plateau using WRF forced by bias-corrected CESM. *Atmospheric Research*, *286*, 106670. https://doi.org/10.1016/j.atmosres.2023.106670

Mann, H. B. (1945). Nonparametric tests against trend. *Econometrica: Journal of the Econometric Society*, *13*(3), 245–259. https://doi.org/10.2307/1907187

Mukul Tewari, N., Tewari, M., Chen, F., Wang, W., Dudhia, J., LeMone, M., et al. (2004). Implementation and verification of the unified NOAH land surface model in the WRF model. In *20th Conference on Weather Analysis and Forecasting/16th Conference on Numerical Weather Prediction* (Formerly Paper Number 17.5) (pp. 11–15).

Neelin, J. D., Martinez-Villalobos, C., Stechmann, S. N., Ahmed, F., Chen, G., Norris, J. M., et al. (2022). Precipitation extremes and water vapor. *Current Climate Change Reports*, *8*(1), 17–33. https://doi.org/10.1007/s40641-021-00177-z

Neelin, J. D., Peters, O., & Hales, K. (2009). The transition to strong convection. *Journal of the Atmospheric Sciences*, *66*(8), 2367–2384. https://doi.org/10.1175/2009jas2962.1

Nie, J., Sobel, A. H., Shaevitz, D. A., & Wang, S. (2018). Dynamic amplification of extreme precipitation sensitivity. *Proceedings of the National Academy of Sciences*, *115*(38), 9467–9472. https://doi.org/10.1073/pnas.1800357115

Nie, Y., & Sun, J. (2022). Moisture sources and transport for extreme precipitation over Henan in July 2021. *Geophysical Research Letters*, *49*, e2021GL097446. https://doi.org/10.1029/2021GL097446

Niu, X., Tang, J., Chen, D., Wang, S., & Ou, T. (2021). Elevation-dependent warming over the Tibetan plateau from an ensemble of CORDEX-EA regional climate simulations. *Journal of Geophysical Research: Atmospheres*, *126*, e2020JD033997. https://doi.org/10.1029/2020JD033997

O'Gorman, P. A. (2015). Precipitation extremes under climate change. *Current Climate Change Reports*, *1*(2), 49–59. https://doi.org/10.1007/s40641-015-0009-3

O'Gorman, P. A., & Schneider, T. (2009). The physical basis for increases in precipitation extremes in simulations of 21st-century climate change. *Proceedings of the National Academy of Sciences of the United States of America*, *106*(35), 14773–14777. https://doi.org/10.1073/pnas.0907610106

Park, I.-H., & Min, S.-K. (2017). Role of convective precipitation in the relationship between subdaily extreme precipitation and temperature. *Journal of Climate*, *30*(23), 9527–9537. https://doi.org/10.1175/JCLI-D-17-0075.1

Pfahl, S., O'Gorman, P. A., & Fischer, E. M. (2017). Understanding the regional pattern of projected future changes in extreme precipitation. *Nature Climate Change*, *7*(6), 423–427. https://doi.org/10.1038/nclimate3287

Pichelli, E., Coppola, E., Sobolowski, S., Ban, N., Giorgi, F., Stocchi, P., et al. (2021). The first multi-model ensemble of regional climate simulations at kilometer-scale resolution part 2: Historical and future simulations of precipitation. *Climate Dynamics*, *56*(11–12), 3581–3602. https://doi.org/10.1007/s00382-021-05657-4

Prein, A. F., Langhans, W., Fosser, G., Ferrone, A., Ban, N., Goergen, K., et al. (2015). A review on regional convection-permitting climate modeling: Demonstrations, prospects, and challenges. *Reviews of Geophysics*, *53*, 323–361. https://doi.org/10.1002/2014RG000475

Prein, A. F., Rasmussen, R. M., Ikeda, K., Liu, C., Clark, M. P., & Holland, G. J. (2017). The future intensification of hourly precipitation extremes. *Nature Climate Change*, *7*(1), 48–52. https://doi.org/10.1038/nclimate3168

Qiu, J. (2008). China: The third pole. *Nature*, *454*(7203), 393–397. https://doi.org/10.1038/454393a

21698996, 2023, 18, Downloaded from https://agupubs.onlinelibrary.wiley.com/doi/10.1029/2023JD039062 by Goteborgs, Wiley Online Library on [12/09/2023]. See the Terms and Conditions (https://onlinelibrary.wiley.com/terms-and-conditions) on Wiley Online Library for rules of use; OA articles are governed by the applicable Creative Commons License

10.1029/2023JD039062

Sen, P. K. (1968). Estimates of the regression coefficient based on Kendall's tau. *Journal of the American Statistical Association*, *63*(324), 1379–1389. https://doi.org/10.1080/01621459.1968.10480934

Shaw, S. B., Royem, A. A., & Riha, S. J. (2011). The relationship between extreme hourly precipitation and surface temperature in different hydroclimatic regions of the United States. *Journal of Hydrometeorology*, *12*(2), 319–325. https://doi.org/10.1175/2011jhm1364.1

Skamarock, W. C., Klemp, J. B., Dudhia, J., Gill, D. O., Liu, Z., Berner, J., et al. (2019). A description of the advanced research WRF model version 4 [Software]. National Center for Atmospheric Research, *145*, 145. https://doi.org/10.5065/1dfh-6p97

Sugiyama, M., Shiogama, H., & Emori, S. (2010). Precipitation extreme changes exceeding moisture content increases in MIROC and IPCC climate models. *Proceedings of the National Academy of Sciences of United States of America*, *107*(2), 571–575. https://doi.org/10.1073/pnas.0903186107

Tandon, N. F., Zhang, X., & Sobel, A. H. (2018). Understanding the dynamics of future changes in extreme precipitation intensity. *Geophysical Research Letters*, *45*, 2870–2878. https://doi.org/10.1002/2017GL076361

Thompson, G., Field, P. R., Rasmussen, R. M., & Hall, W. D. (2008). Explicit forecasts of winter precipitation using an improved bulk microphysics scheme. Part II: Implementation of a new snow parameterization. *Monthly Weather Review*, *136*(12), 5095–5115. https://doi.org/10.1175/2008mwr2387.1

Tramblay, Y., El Adlouni, S., & Servat, E. (2013). Trends and variability in extreme precipitation indices over Maghreb countries. *Natural Hazards and Earth System Sciences*, *13*(12), 3235–3248. https://doi.org/10.5194/nhess-13-3235-2013

Trenberth, K. (2011). Changes in precipitation with climate change. *Climate Research*, *47*(1), 123–138. https://doi.org/10.3354/cr00953

Trenberth, K. E. (1999). Conceptual framework for changes of extremes of the hydrological cycle with climate change. In *Weather and climate extremes* (pp. 327–339). Springer. https://doi.org/10.1007/978-94-015-9265-9_18

Trenberth, K. E., Zhang, Y., & Gehne, M. (2017). Intermittency in precipitation: Duration, frequency, intensity, and amounts using hourly data. *Journal of Hydrometeorology*, *18*(5), 1393–1412. https://doi.org/10.1175/jhm-d-16-0263.1

Utsumi, N., Seto, S., Kanae, S., Maeda, E. E., & Oki, T. (2011). Does higher surface temperature intensify extreme precipitation? *Geophysical Research Letters*, *38*, L16708. https://doi.org/10.1029/2011GL048426

Ward, P. J., Blauhut, V., Bloemendaal, N., Daniell, J. E., De Ruiter, M. C., Duncan, M. J., et al. (2020). Review article: Natural hazard risk assessments at the global scale. *Natural Hazards and Earth System Sciences*, *20*(4), 1069–1096. https://doi.org/10.5194/nhess-20-1069-2020

Wasko, C., & Sharma, A. (2017). Global assessment of flood and storm extremes with increased temperatures. *Scientific Reports*, *7*(1), 7945. https://doi.org/10.1038/s41598-017-08481-1

Wehner, M., Lee, J., Risser, M., Ullrich, P., Gleckler, P., & Collins, W. D. (2021). Evaluation of extreme sub-daily precipitation in high-resolution global climate model simulations. *Philosophical Transactions of the Royal Society A: Mathematical, Physical & Engineering Sciences*, *379*(2195), 20190545. https://doi.org/10.1098/rsta.2019.0545

Weisman, M. L., Skamarock, W. C., & Klemp, J. B. (1997). The resolution dependence of explicitly modeled convective systems. *Monthly Weather Review*, *125*(4), 527–548. https://doi.org/10.1175/1520-0493(1997)125<0527:TRDOEM>2.0.CO;2

Xiao, C., Wu, P., Zhang, L., & Song, L. (2016). Robust increase in extreme summer rainfall intensity during the past four decades observed in China. *Scientific Reports*, *6*(1), 38506. https://doi.org/10.1038/srep38506

Xiong, J., Yong, Z., Wang, Z., Cheng, W., Li, Y., Zhang, H., et al. (2019). Spatial and temporal patterns of the extreme precipitation across the Tibetan plateau (1986–2015). *Water*, *11*(7), 1453. https://doi.org/10.3390/w11071453

Yang, K., Wu, H., Qin, J., Lin, C., Tang, W., & Chen, Y. (2014). Recent climate changes over the Tibetan plateau and their impacts on energy and water cycle: A review. *Global and Planetary Change*, *112*, 79–91. https://doi.org/10.1016/j.gloplacha.2013.12.001

Yang, T., Hao, X., Shao, Q., Xu, C.-Y., Zhao, C., Chen, X., & Wang, W. (2012). Multi-model ensemble projections in temperature and precipitation extremes of the Tibetan Plateau in the 21st century. *Global and Planetary Change*, *80*, 1–13. https://doi.org/10.1016/j.gloplacha.2011.08.006

Yang, Z. L., Dickinson, R., Henderson-Sellers, A., & Pitman, A. (1995). Preliminary study of spin-up processes in land surface models with the first stage data of Project for Intercomparison of Land Surface Parameterization Schemes Phase 1 (a). *Journal of Geophysical Research*, *100*(D8), 16553–16578. https://doi.org/10.1029/95JD01076

Yao, T., Thompson, L. G., Mosbrugger, V., Zhang, F., Ma, Y., Luo, T., et al. (2012). Third pole environment (TPE). *Environmental Development*, *3*, 52–64. https://doi.org/10.1016/j.envdev.2012.04.002

Yao, T., Xue, Y., Chen, D., Chen, F., Thompson, L., Cui, P., et al. (2019). Recent third Pole's rapid warming accompanies cryospheric melt and water cycle intensification and interactions between monsoon and environment: Multidisciplinary approach with observations, modeling, and analysis. *Bulletin of the American Meteorological Society*, *100*(3), 423–444. https://doi.org/10.1175/bams-d-17-0057.1

Yong, Z., Xiong, J., Wang, Z., Cheng, W., Yang, J., & Pang, Q. (2021). Relationship of extreme precipitation, surface air temperature, and dew point temperature across the Tibetan Plateau. *Climatic Change*, *165*(1–2), 41. https://doi.org/10.1007/s10584-021-03076-2

You, Q., Fraedrich, K., Ren, G., Ye, B., Meng, X., & Kang, S. (2012). Inconsistencies of precipitation in the eastern and central Tibetan Plateau between surface adjusted data and reanalysis. *Theoretical and Applied Climatology*, *109*(3–4), 485–496. https://doi.org/10.1007/s00704-012-0594-1

You, Q., Kang, S., Aguilar, E., & Yan, Y. (2008). Changes in daily climate extremes in the eastern and central Tibetan Plateau during 1961–2005. *Journal of Geophysical Research*, *113*, D07101. https://doi.org/10.1029/2007JD009389

Yu, R., Xu, Y., Zhou, T., & Li, J. (2007). Relation between rainfall duration and diurnal variation in the warm season precipitation over central eastern China. *Geophysical Research Letters*, *34*, L13703. https://doi.org/10.1029/2007GL030315

Zhang, B., He, Y., Ren, Y., Huang, B., Peng, Y., Wang, S., & Guan, X. (2023). The influence of the precipitation recycling process on the shift to heavy precipitation over the Tibetan Plateau in the summer. *Frontiers in Earth Science*, *11*, 1078501. https://doi.org/10.3389/feart.2023.1078501

Zhou, P., Shao, M., Ma, M., Ou, T., & Tang, J. (2022). WRF gray-zone dynamical downscaling over the Tibetan plateau during 1999–2019: Model performance and added value. *Climate Dynamics*, *61*(3–4), 1371–1390. https://doi.org/10.1007/s00382-022-06631-4

Zhou, T., & Zhang, W. (2021). Anthropogenic warming of Tibetan Plateau and constrained future projection. *Environmental Research Letters*, *16*(4), 044039. https://doi.org/10.1088/1748-9326/abede8

Zhu, X., Wei, Z., Dong, W., Wen, X., Zheng, Z., Chen, G., & Liu, Y. (2019). Projected temperature and precipitation changes on the Tibetan plateau: Results from dynamical downscaling and CCSM4. *Theoretical and Applied Climatology*, *138*(1–2), 861–875. https://doi.org/10.1007/s00704-019-02841-9

21698996, 2023, 18, Downloaded from https://agupubs.onlinelibrary.wiley.com/doi/10.1029/2023JD039062 by Goteborgs, Wiley Online Library on [12/09/2023]. See the Terms and Conditions (https://onlinelibrary.wiley.com/terms-and-conditions) on Wiley Online Library for rules of use; OA articles are governed by the applicable Creative Commons License